JEM Journal of Experimental Medicine

BRIEF DEFINITIVE REPORT

Chronic T cell proliferation in brains after stroke could interfere with the efficacy of immunotherapies

Steffanie Heindl[1], Alessio Ricci[1], Olga Carofiglio[1], Qihui Zhou[2], Thomas Arzberger[3,4], Nikolett Lenart[5], Nicolai Franzmeier[1], Tibor Hortobagyi[6], Peter T. Nelson[7], Ann M. Stowe[7], Adam Denes[5], Dieter Edbauer[2,8], and Arthur Liesz[1,8]

Neuroinflammation is an emerging focus of translational stroke research. Preclinical studies have demonstrated a critical role for brain-invading lymphocytes in post-stroke pathophysiology. Reducing cerebral lymphocyte invasion by anti-CD49d antibodies consistently improves outcome in the acute phase after experimental stroke models. However, clinical trials testing this approach failed to show efficacy in stroke patients for the chronic outcome 3 mo after stroke. Here, we identify a potential mechanistic reason for this phenomenon by detecting chronic T cell accumulation—evading the systemic therapy—in the post-ischemic brain. We observed a persistent accumulation of T cells in mice and human autopsy samples for more than 1 mo after stroke. Cerebral T cell accumulation in the post-ischemic brain was driven by increased local T cell proliferation rather than by T cell invasion. This observation urges re-evaluation of current immunotherapeutic approaches, which target circulating lymphocytes for promoting recovery after stroke.

Introduction

Stroke is one of the leading causes of death and permanent disability worldwide (World Health Organization, 2017). Despite the enormous medical need, specific therapies for stroke patients are still limited to vascular recanalization approaches within the acute phase after stroke (Emberson et al., 2014; Fiehler and Gerloff, 2015; Hacke et al., 2008). In the search for alternative therapeutic strategies, post-stroke neuroinflammation has come into focus in current translational stroke research (Iadecola and Anrather, 2011). Neuroinflammation after stroke is a crucial pathomechanism contributing to secondary brain injury, neurodegeneration, and recovery (Iadecola and Anrather, 2011; Moskowitz et al., 2010). While different leukocyte cell populations have been implicated in the neuroinflammatory response to stroke, T cells have been consistently shown to be a key cell population driving secondary brain injury (Chamorro et al., 2012; Macrez et al., 2011). Consequently, several therapeutic strategies targeting the brain invasion of lymphocytes have been tested using antibodies against key adhesion molecules or by reducing the number of circulating lymphocytes (Chamorro et al., 2012; Cramer et al., 2019a).

A prominent and controversial example of this translational approach is the use of anti-CD49d antibodies (Natalizumab), which reduces the invasion of circulating lymphocytes to the brain by blocking a key adhesion molecule. The repurposing of this drug used for patients with multiple sclerosis improved outcome in the acute phase after experimental stroke in the majority of preclinical studies (Becker et al., 2001; Langhauser et al., 2014; Liesz et al., 2011; Neumann et al., 2015; Relton et al., 2001), which was validated in a first-ever multicenter, randomized preclinical trial (Llovera et al., 2015). In a first phase 2 clinical trial (ACTION), Natalizumab treatment significantly improved functional outcome (modified Rankin scale) in the subacute phase (30 d), but this effect was not evident anymore in the chronic phase (90 d; Elkins et al., 2017). Correspondingly, a follow-up phase 2b trial (ACTION-II) also did not report any improvement with Natalizumab treatment in the stroke outcome at 90 d (Elkind et al., 2020).

Failed translations from promising experimental studies to clinical trials are commonly attributed to differences in study design, target engagement, or lack of statistical robustness of the preclinical findings (Endres et al., 2008; Howells et al., 2014; Macleod et al., 2014). However, the efficacy of Natalizumab in preclinical models has been extraordinarily well characterized, and clinical trials have closely mimicked the efficient

[1]Institute for Stroke and Dementia Research, University Hospital, Ludwig Maximilians University Munich, Munich, Germany; [2]German Center for Neurodegenerative Diseases, Munich, Germany; [3]Department of Psychiatry and Psychotherapy, University Hospital, Ludwig Maximilians University Munich, Munich, Germany; [4]Center for Neuropathology and Prion Research, Ludwig Maximilians University Munich, Munich, Germany; [5]Momentum Laboratory of Neuroimmunology, Institute of Experimental Medicine, Budapest, Hungary; [6]ELKH-DE Cerebrovascular and Neurodegenerative Research Group, Department of Neurology, University of Debrecen, Debrecen, Hungary; [7]University of Kentucky, Lexington, KY; [8]Munich Cluster for Systems Neurology (SyNergy), Munich, Germany.

Correspondence to Arthur Liesz: arthur.liesz@med.uni-muenchen.de.

therapeutic approaches in animal models in the design of the treatment regimen and investigated outcome parameters, with the exception of analyzing different time points after stroke: Clinical trials analyzed the chronic phase after stroke as the primary endpoint in contrast to preclinical studies, where only the acute phase was studied. Therefore, we took a reverse translational approach and tested whether the design of the clinical trials—analyzing chronic stroke outcome between patient groups with similar baseline characteristics after stroke—would have been efficacious in the murine experimental stroke model. Confirming a lack of efficacy on chronic post-stroke recovery also in animal models further prompted us to study the potentially underlying mechanisms of the diverging effects in acute versus chronic phases after stroke.

Results and discussion

Natalizumab treatment does not improve post-stroke recovery and neuronal plasticity

To model the clinical study design of Natalizumab treatment for stroke from the two clinical trials in an animal model, we used a photothrombotic stroke (PT) model resulting in equal lesion volumes and behavioral deficits in both treatment groups at the acute phase, corresponding to the equal characteristics of the study populations with Natalizumab or control treatment in the clinical trials. Mice of mixed sex then received anti-CD49d or an isotype control antibody i.p. 2 h after stroke, followed by injections every second week over a period of 3 mo, based on previous reports and the pharmacokinetic analyses of cellular anti-CD49d saturation (Fig. S1, A–D). We used a panel of in vivo imaging techniques for cortical plasticity, behavior tests, the assessment of lesion size and synaptic plasticity, which were proven to sensitively detect therapeutic effects on chronic post-stroke recovery (Cramer et al., 2019b; Cserép et al., 2020; Sadler et al., 2020). Anti-CD49d treatment did not improve long-term lesion involution based on in vivo widefield imaging (Fig. 1, A and B; and Fig. S1 D) and also had no effect on histologically quantified lesion volumes after PT as well as in an independent stroke model of distal middle cerebral artery occlusion (dMCAo) used in the majority of previous reports on the effects in the acute post-stroke phase (Fig. 1 C and Fig. S1 E). Moreover, recovery of behavior deficits using a well-established multiparameter neuroscore (Llovera et al., 2015) and cylinder test (Llovera et al., 2014) also did not differ between treatment groups throughout the observation period of 3 mo after stroke (Fig. 1 D). Additionally, we examined functional neuronal connectivity using in vivo widefield calcium imaging. We observed equal network disturbances in pairwise comparisons of functional cortical areas in both treatment groups after stroke (Fig. 1 E). Moreover, we did not detect anti-CD49d-associated improvement in neuronal network connectivity after stroke neither within the ischemic hemisphere nor across homotopic areas of both brain hemispheres (Fig. 1 F). Correspondingly, quantification of synaptic spine density as a marker of synaptic plasticity at 3 mo after stroke did not reveal a difference between treatment groups, which were both returned to baseline levels (naive). These results clearly indicate a lack of efficacy for anti-CD49d to improve functional recovery in the chronic post-stroke phase in two preclinical stroke models, which is comparable to the outcome of the clinical trials testing the efficacy of Natalizumab in stroke patients (Elkind et al., 2020; Elkins et al., 2017; Liesz et al., 2011; Llovera et al., 2015).

Anti-CD49d only transiently reduces cerebral lymphocyte counts after stroke

Therefore, we next aimed to analyze the biological efficacy of anti-CD49d treatment in reducing long-term lymphocyte invasion to the injured brain, which could not be studied in the clinical trials. To this end, we performed quantitative flow cytometric analyses at acute and chronic time points after stroke. Corresponding to previous studies by us and others, anti-CD49d significantly decreased cerebral lymphocyte invasion at the acute phase in male and female animals (Fig. 2 A and Fig. S3 A). In contrast, no difference in cerebral leukocyte count was detectable between treatment groups at 1 mo after stroke for any of the T cell subtypes, which we quantified in a multidimensional flow cytometric analysis (Fig. 2, B and C). Interestingly, we found T cells among leukocyte populations to specifically accumulate in the chronic phase after stroke (Fig. S2). Next, we performed immunofluorescence labeling of $CD3^+$ T cells to analyze the spatial distribution of T cells after stroke. Consistent with our flow cytometric results and a previous report (Doyle et al., 2015), we found dense T cell accumulation within the chronic lesion but did not detect a difference in intralesional T cell density between control or anti-CD49d–treated groups at 28 d after stroke (Fig. 2 D). We analyzed the spatial clustering of T cells by calculating the Clark–Evans agglomeration index (R index), which indicates cell clustering for an $R < 1$ (Fig. 2 E). Interestingly, the R index ranged between 0.3 and 0.7 for both acute (day 7) as well as for chronic (day 28) time points, regardless of treatment groups. Additionally, chronic T cell accumulation and their local clustering was confirmed in the dMCAo stroke model for both treatment groups (Fig. S3 B). Thus, the chronic accumulation of T cells in the post-ischemic brain associates with local clustering of T cells likely due to local, intracerebral proliferation. This finding could potentially explain the difference in treatment efficacy of anti-CD49d between the acute stroke outcome (with transiently reduced cerebral T cell invasion) and long-term recovery. Taken together, our approach to monitor the treatment efficacy of anti-CD49d for chronic recovery in two independent stroke models could have predicted the inefficacy of Natalizumab in clinical stroke trials. Moreover, this first-ever analysis of long-term effects of anti-CD49d treatment on the cerebral lymphocyte pool provides a mechanistic rationale for the futile treatment effects in the chronic post-stroke phase.

T cells proliferate intracerebrally after stroke

We next aimed to distinguish chronic recruitment versus local proliferation as the potential cause of the chronic lymphocyte accumulation in the post-stroke brain. Therefore, we administered 5-ethynyl-2′-deoxyuridine (EdU), a thymidine analogue labeling proliferating cells, in the drinking water over a 7-d time period, starting either the day of surgery (days 0–7) or 3 wk later

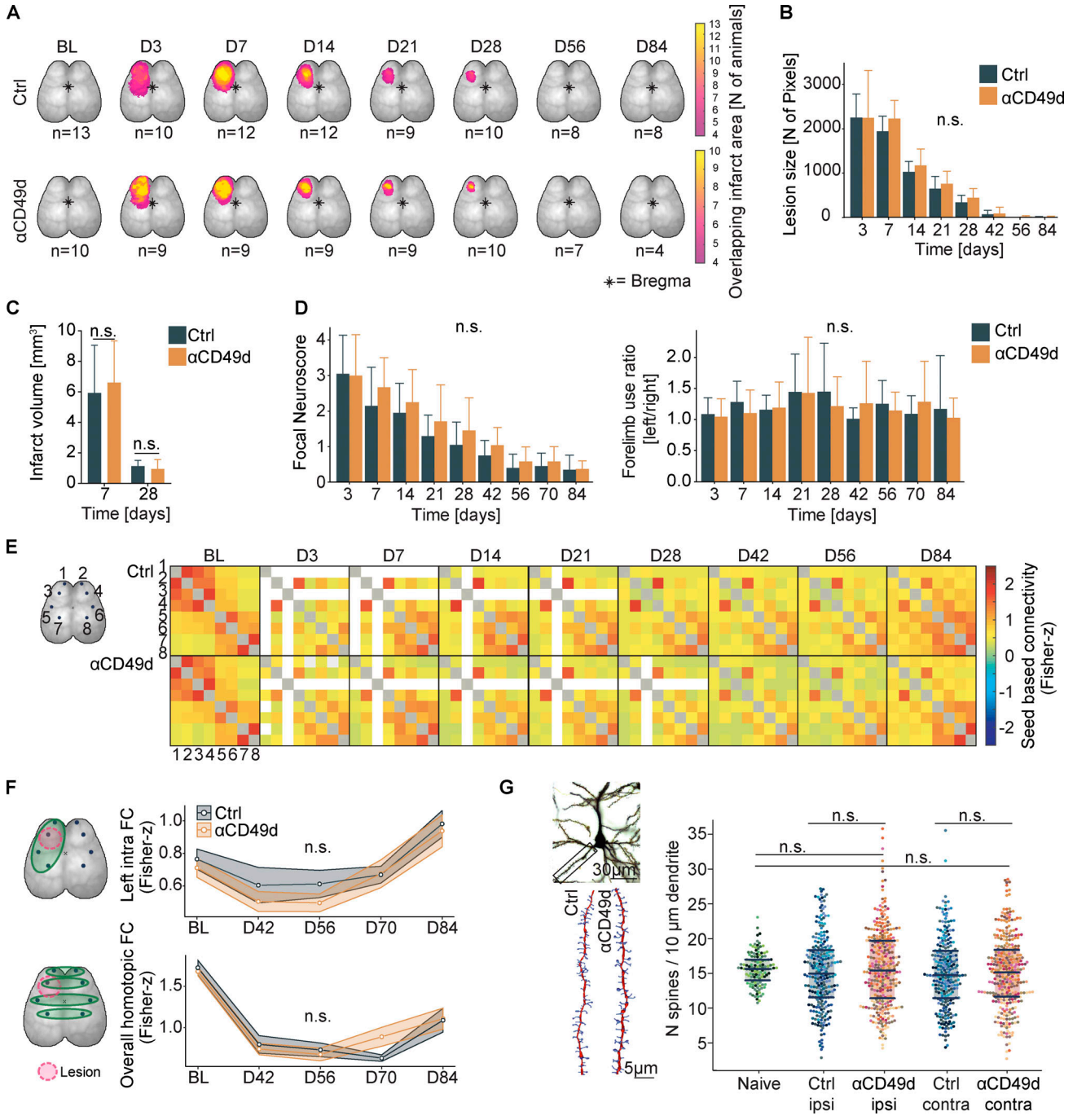

Figure 1. **Longitudinal evaluation of post-stroke recovery in mice receiving anti-CD49d treatment. (A)** The lesion area based on autofluorescence after stroke of individual animals was superimposed to depict the lesion throughout the observation period of 84 d in Thy1-GCaMP6s animals. The color code indicates the sum of overlapping lesion pixels of individual mice per acquisition time point. Data were generated in two independent experiments. BL, baseline; D, day. **(B)** Quantification of the number of autofluorescent pixels seen in calcium imaging of Thy1-GCaMP6s animals. Control (Ctrl): *n* = 10, anti-CD49d: *n* = 13, P = 0.716. Data are shown as mean ± SD, linear-mixed-models, group-by-time interaction. Data were generated in two independent experiments. **(C)** The lesion volume was quantified at 7 and 28 d after stroke and shows no difference between treatment groups. Control 7 d: *n* = 6, control 28 d: *n* = 11, anti-CD49d 7 d: *n* = 5, anti-CD49d 28 d: *n* = 8, all WT animals. Data are shown as mean ± SD. Ordinary one-way ANOVA + Tukey's post-hoc test. Data were generated in at least three independent experiments per time point. **(D)** Evaluation of the multi-parameter neuroscore and cylinder test shows no difference between treatment groups. Control: *n* = 10, anti-CD49d: *n* = 13, P (neuroscore) = 0.560, P (cylinder) = 0.691. Data are shown as median ± SE, linear-mixed models, group-by-time interaction. Data were generated in two independent experiments in Thy1-GCaMP6s animals. **(E)** Illustrative pixelmaps show the group-wise averaged seed-based FC between eight seeds representing functional cortical areas over an observation period of 84 d after stroke by longitudinal in vivo calcium imaging: 1, left rostral forelimb; 2, right rostral forelimb; 3, left caudal forelimb; 4, right caudal forelimb; 5, left forelimb sensory area; 6, right forelimb sensory area; 7, left hindlimb sensory area; 8, right hindlimb sensory area.. Gray squares indicate excluded seed autocorrelation, and white squares indicate excluded seeds due to the stroke lesion, when excluded in more than three animals. Data are shown as Fisher z-transformed connectivity scores and were generated in two independent experiments in Thy1-GCaMP6s animals. **(F)** Schematic illustration for longitudinal in vivo widefield calcium imaging acquisition; left intrahemispheric and whole cortex homotopic FC

of the eight previously defined functional areas. Time course of left intrahemispheric FC (intra FC; P = 0.127) and overall homotopic FC (P = 0.295). Data are shown as median ± SE, linear-mixed models, group-by-time interaction. Data were generated in two independent experiments in Thy1-GCaMP6s animals. **(G)** Representative images of a Golgi-Cox–stained pyramidal neuron layer II/III in a naive animal (scale bar = 30 µm) and 3D reconstruction of pyramidal neuron dendrites (red) with dendritic spines (blue, scale bar = 5 µm). Dendritic spines were quantified in layer II/III in naive (untreated) animals and 84 d after stroke in stroke ipsi- and contralateral hemispheres. Naive: *n* = 5, control: *n* = 10, anti-CD49d: *n* = 13. Data are shown as median ± interquartile range. Wilcoxon rank-sum test with continuity correction and Bonferroni correction for multiple comparisons were used. Data were generated in at least two independent experiments. All data in this figure were obtained in a mixed-sex cohort (anti-CD49d: four male, nine female; control: three male, seven female), except for C (only male mice).

(days 21–28). Then, the rate of proliferating T cells was determined in blood, spleen, and the ischemic brain hemisphere after acute (day 7) or chronic (day 28) EdU labeling in untreated mice (Fig. 3 A). As expected for the acute inflammatory response, we observed an increase in the proliferation rate (percentage of EdU^+ cells) for cerebral T cells in comparison to splenic and blood T cells at 7 d after stroke. Surprisingly, the proliferation rate in the chronic phase was still significantly (more than twofold) increased for the cerebral T cell population compared with peripheral organs. In contrast, using systemic antibody labeling of circulating T cells over 3 d (days 25–28), we detected only a small number of T cells still de novo–invading the brain in the chronic phase after stroke (Fig. S3 C). To additionally confirm the local proliferation of cerebral T cells, we analyzed histologically the expression of the direct proliferation marker Ki67 to quantify the percentage of proliferating T cells within the chronic stroke lesion (Fig. 3 B). We found independent of the treatment group a substantial number of >5% $Ki67^+$ T cells, confirming the local intralesional proliferation of T cells 28 d after PT (Fig. 3 C), which was also confirmed in the dMCAo stroke model with comparable findings (Fig. S3 D). These results suggest that—regardless of anti-CD49d treatment—sustained and local proliferation of T cells in the post-stroke brain drives chronic cerebral T cell accumulation after stroke.

Evidence for chronic T cell accumulation in human brain autopsy samples

To verify chronic T cell accumulation after stroke in brains of human stroke patients, we obtained 10 individual samples from two brain banks (Lexington and Debrecen) of six individual stroke patients dying during the acute and chronic phase after confirmed cerebral ischemia and excluding other brain disorders or immunological or inflammatory diseases (Table S1). The area covering the ischemic lesion within the samples was identified based on H&E staining for quantitative analyses. Using immunohistochemical staining, we detected $CD3^+$ T cells in all 10 human brain samples (Fig. 3 D). The number of detected T cells ranged from ∼300 to >9,000 cells/cm^2 of tissue section, with an average of 80% located within the lesion area. Additionally, the spatial distribution of T cells within the stroke lesions was determined and showed strong local clustering, with an R index ranging from 0.28 to 0.55 (Fig. 3 E). A Spearman correlation analysis for T cell density and time since stroke revealed a highly significant positive association. These results clearly demonstrate that T cells accumulate chronically and cluster locally in the ischemic lesion of human stroke patients. We additionally performed immunofluorescence staining for $CD3^+$ T cells and Ki67 in the most chronically collected patient sample (124 d after stroke) and detected double-positive cells (Fig. 3 F), confirming that the phenomenon of local, intracerebral proliferation of T cells in the chronic phase after stroke also applies to human stroke patients.

Taken together, we describe here chronic T cell accumulation most likely due to local proliferation after ischemic stroke in mice and human brains, constituting a previously unrecognized potential confounder for immunotherapeutic studies after ischemic stroke. None of the current pharmacological approaches block completely the cerebral invasion of T cells after stroke (in contrast to experimental T cell–depletion approaches; Liesz et al., 2009; Liesz et al., 2011) but rather reduce numbers of invading T cells by various degrees (Liesz et al., 2011; Llovera et al., 2015). Therefore, despite the therapeutic intervention, some T cells invade the ischemic brain. Once in the cerebral microenvironment, T cells might become autonomous from the peripheral immune system and establish a tissue-resident population by local proliferation. Here, we confirm chronic T cell accumulation and local proliferation in two independent experimental stroke models (PT and dMCAo). However, further mechanistic studies will be required to explore the biological function and therapeutic implications of this unexpected phenomenon.

For this study, we mainly used the PT model, which induces a pronounced cellular neuroinflammatory response and allows for sensitive analysis of neuromodulatory effects in the chronic recovery phase after stroke (Cotrina et al., 2017; Sadler et al., 2020). Key findings on lesion volume, T cell accumulation, and proliferation have additionally been confirmed in a widely used dMCAo model with similar findings in male and female animals. However, considering previous reports on model differences concerning the extent and dynamics of the neuroinflammatory response to stroke, future clinical trials need to consider not only potentially unexpected long-term effects, as reported in this study, but also potentially drastic differences in the role of neuroinflammation between stroke subtypes regarding lesion location, size, and etiology (Cotrina et al., 2017; Cramer et al., 2019a; Zhou et al., 2013).

As such, our findings have high clinical relevance for many ongoing or planned immunotherapeutic trials in stroke that target circulating lymphocytes, their endothelial adhesion, or cerebral invasion. According to the ClinicalTrials.gov registry of clinical intervention trials, more than 40 trials are exploring such strategies with pending outcome as of March 2021. The therapeutic approaches in these studies cover a broad range of potential therapies, including (autologous) cell therapies, polarization of T cell responses, or modulating lymphocyte migration. Several of these studies use repurposing of drugs that

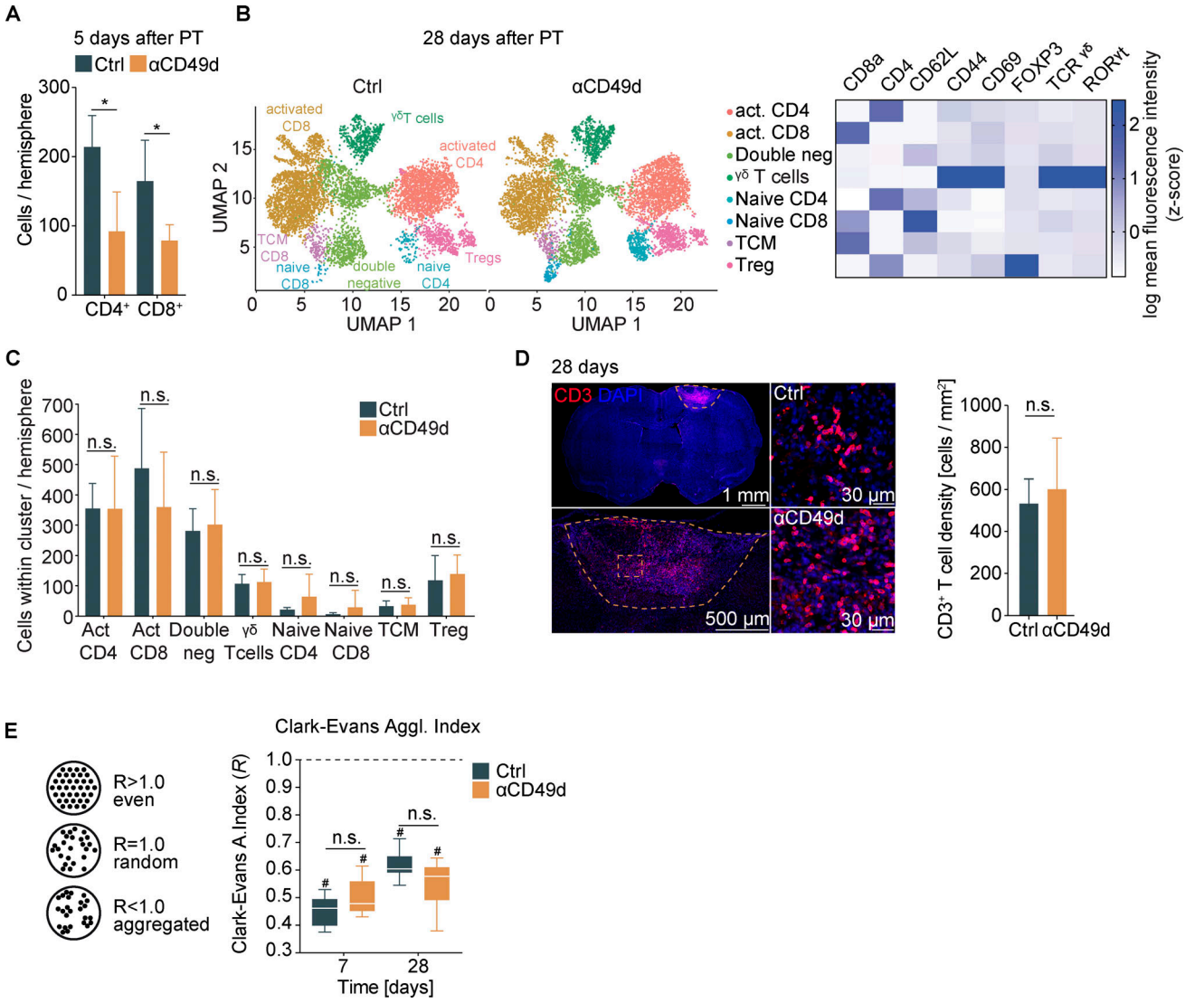

Figure 2. **T cells chronically accumulate in the post-ischemic brain independent of anti-CD49d treatment. (A)** Flow cytometric quantification of CD4⁺ T helper cells and CD8⁺ cytotoxic T cells per ipsilateral stroke hemisphere at 5 d after stroke. *n* = 5 per group. Data are shown as mean ± SD, unpaired *t* test with Holm–Sidak's post-hoc test. Data were generated in two independent experiments in WT animals. **(B)** Quantification of T cell subtypes by multidimensional flow cytometry 28 d after stroke from the ipsilateral stroke hemisphere was achieved by dimensionality reduction using UMAP (Uniform Manifold Approximation and Projection). The individual clusters were identified as CD3⁺ T cell subtypes by the MFI of CD8a, CD4, CD62L, CD44, CD69, Foxp3, γδ TCR, and RORγt, as shown in the heatmap on the right, including activated (act.) CD4⁺ T helper cells (CD4⁺CD69⁺CD62L⁻), activated CD8⁺ cytotoxic T cells (CD8⁺CD69⁺CD62L⁻ RORγt⁺), double-negative T cells (CD4⁻CD8⁻), γδ T cells (TCRγδ⁺CD44⁺CD69⁺), naive CD4⁺ T helper cells (CD4⁺CD69⁻CD62L⁺), naive CD8⁺ cytotoxic T cells (CD8⁺CD69⁻CD62L⁺), central memory T cells (TCM; CD8⁺CD69⁻CD62L⁺CD44⁺), and regulatory T cells (Treg; CD4⁺FOXP3⁺). **(C)** Quantification of numbers of T cell subtypes per cluster in the ipsilateral stroke hemisphere shown in B. Control: *n* = 5, anti-CD49d: *n* = 7. Data are shown as mean ± SD; unpaired *t* test and Holm–Sidak post-hoc test. The data were generated in three independent experiments in WT animals. **(D)** Representative immunofluorescence images of CD3⁺ T cells in the brain 28 d after stroke of the whole section with demarcation of the lesion (upper left, scale bar = 1 mm), the lesion area (lower left, scale bar = 500 µm), and an area within the lesion from control and anti-CD49d animals (right, scale bars = 30 µm). The T cell density within the lesion (cells per square millimeter) showed no difference between groups. Control: *n* = 11, anti-CD49d: *n* = 8. Data are shown as mean ± SD; unpaired *t* test. The data were generated in at least three independent experiments in WT animals. **(E)** Schematic representation of the R index for describing cell clustering (left) and the R index for CD3⁺ T cells within the lesion at 7 and 28 d after stroke for both treatment groups (right). Control 7 d: *n* = 6, control 28 d: *n* = 11, anti-CD49d 7 d: *n* = 5, anti-CD49d 28 d: *n* = 8. Data are shown as median ± interquartile range. *, P < 0.05; #, P (clustered [R < 1]) <0.0001; ordinary one-way ANOVA + Tukey's post-hoc test. Data were generated in at least three independent experiments per time point in WT animals.

have been established and approved for multiple sclerosis, a disease that not only differs drastically in its pathogenesis but also has distinct neuroimmunological features. However, the differences between acute ischemic lesions and chronic autoimmune brain disorders have not yet been fully characterized and may pose a threat to the success of immunotherapeutic stroke trials.

In light of these findings, current clinical trials targeting lymphocyte migration or brain recruitment (lymphocyte-depleting antibodies, fingolimod, and cell therapy approaches)

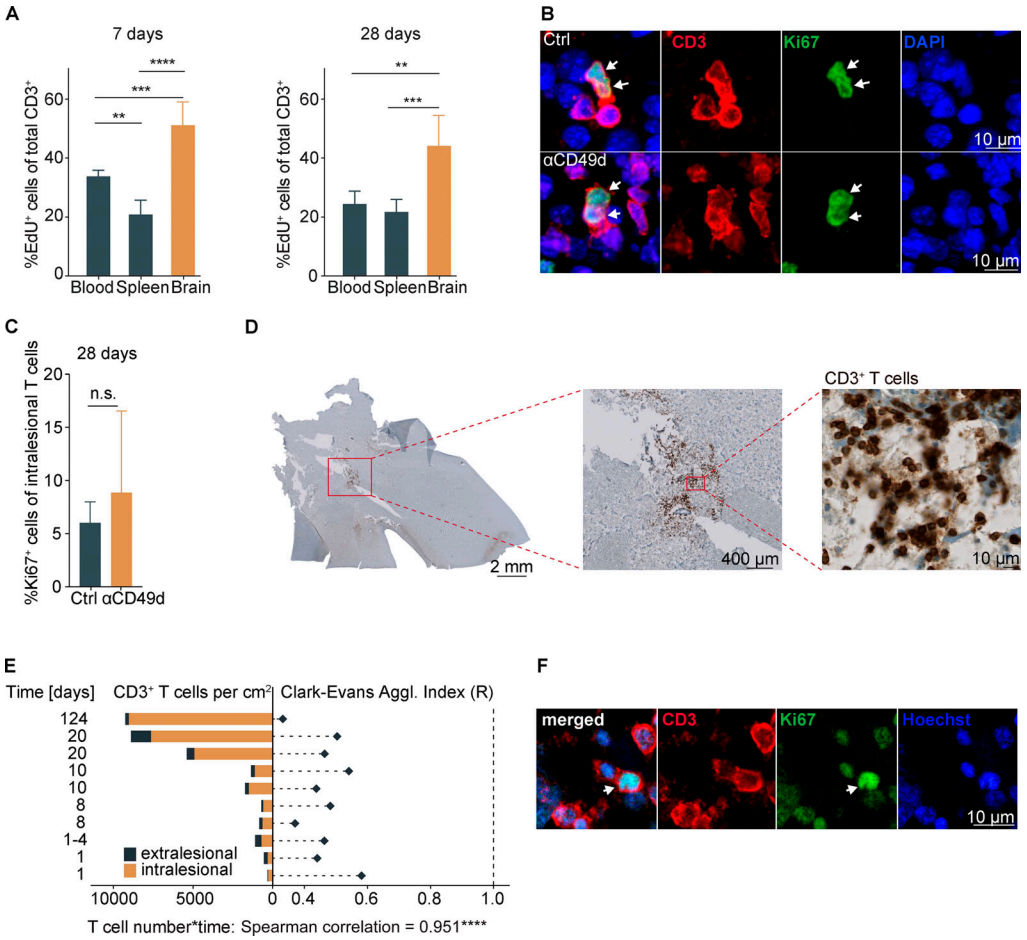

Figure 3. **T cells chronically proliferate in the postischemic brain in mice and stroke patients. (A)** The percentage of EdU+ T cells was quantified by flow cytometry in the spleen, blood, and ipsilateral stroke hemisphere at day 7 and day 28 after stroke (n = 5 per group). Data are shown as mean ± SD; ordinary one-way ANOVA and Tukey's post-hoc test. Two independent experiments per time point were performed in WT animals. **(B)** Representative images show immunofluorescence staining for CD3 and Ki67 within the lesion area for the detection of intracerebral T cell proliferation 28 d after stroke in both treatment groups (upper row, control; lower row, anti-CD49d). Arrows point to CD3 and Ki67 double-positive T cells. Scale bars = 10 µm. **(C)** Quantification of the percentage of Ki67+ T cells from (B) within the lesion 28 d after stroke showed no difference between the treatment groups. control: n = 11, anti-CD49d: n = 8. Data are shown as mean ± SD. Unpaired t test. The data were generated in at least three independent experiments in WT animals. **(D)** Representative images are shown for CD3+ DAB staining on consecutive brain sections from a human sample (124 d since stroke onset). Higher magnification images are shown from respective indicated areas. Scale bars: left, 1 mm; middle, 400 µm; right, 10 µm. **(E)** Cell density (cells/square centimeter) of intra- and extralesional CD3 T cells and cell clustering by R index were quantified. P (clustered [R < 1] <0.0001) for all analyzed samples. Correlation analysis (Spearman) between T cell density and time since stroke onset per sample. **(F)** Representative images of immunofluorescence staining for CD3 and Ki67 within the previously histopathologically identified lesion area are shown for the patient samples with the highest detected T cell count (124 d since stroke onset). Arrows point to CD3 and Ki67 double-positive T cells. Scale bar = 10 µm. **, P < 0.01; ***, P < 0.001; ****, P < 0.0001.

need to be fundamentally reconsidered. Mechanisms of chronic neuroinflammation after stroke and the consequences for post-stroke recovery need to be better understood for the rationale design of efficient immunotherapies in stroke.

Materials and methods

Animals

All experiments in this study were conducted in accordance with the national guidelines for animal experiments and approved by the German governmental committees (Regierungpraesidium Oberbayern, Munich, Germany). For flow cytometric and immunohistochemical analyses, the animals were 8–12-wk-old male or female C57BL/6J mice (Charles River Laboratories). For in vivo widefield calcium imaging and dendritic Golgi spine analysis, the animals were 12–15-wk-old male and female C57BL/6J-Tg(Thy1-GCaMP6s)GP4.12Dkim/J (here termed Thy1-GCaMP6s; Dana et al., 2014) heterozygous mice bred at the Institute for Stroke and Dementia Research, Munich (>12 generations back-crossed on C57Bl6/J WT mice). The animals were housed under controlled temperature (22 ± 2°C) with a 12-h light/dark cycle and access to food and water ad libitum. All animal experiments were performed and reported in accordance with the ARRIVE guidelines (Kilkenny et al., 2010).

Stroke surgery

For PT induction, mice were anaesthetized with isoflurane, delivered in a mixture of 30% O_2 and 70% N_2O. Mice were placed

into a stereotactic frame, and body temperature was maintained at 37°C with a mouse warming pad. Dexpanthenol eye ointment was applied to both eyes. Animals received 10 µl/g body weight of 1% Rose Bengal (198250-5g; Sigma-Aldrich) in saline i.p. 5 min before the induction of anesthesia (5% isoflurane). A skin incision was used to expose the skull. Bregma was located, and the lesion location was marked in the left hemisphere (1.5 mm lateral and 1.0 mm rostral to bregma). For in vivo widefield calcium imaging experiments, PT was induced as previously described (Cramer et al., 2019b). In brief, an independent vector analysis was performed based on baseline resting-state imaging, which allowed us to define cortical functional regions as independent components. The independent component in the primary motor cortex was then used to individually define the lesion location for every mouse. Shielding was placed on the skull, allowing a 2.0-mm-diameter circular light exposure over the lesion area. 10 min after Rose Bengal injection, the laser (25 mV output) was applied to the lesion area for 17 min (Cobolt Jive 50, 561 nm power at 25 mV; Fiber Collimation Package: 543 nm, f = 7.66 mm, beam diameter [d] ≈ (4)(0.000561 mm)[7.86 mm/(pi × 0.004 mm)] = 1.4 mm). The sham procedure was performed as described previously but without laser illumination.

dMCAo was performed as previously described (Llovera et al., 2014). Briefly, the mouse was positioned on its side and skin was incised between the ear and the eye. After, the temporal muscle was detached from the bone and a craniotomy was performed on top of the middle cerebral artery. The vessel was permanently coagulated, proximal and distal to the MCA bifurcation, with electrocoagulation forceps. Finally, the muscle was placed back and the wound sutured.

Anti-CD49d antibody treatment

Animals were treated with 300 µg anti-CD49d (clone PS/2, catalog no. BE0071; Bio X Cell) or isotype control (LTF-2, catalog no. BE0090; Bio X Cell) in 0.01 M PBS 2 h after PT induction, followed by injection every second week until termination of the experiment. The treatment groups were assigned after randomization, and experimenters were blinded to group assignment.

Neuroscore

The multiparametric neuroscore was assessed as previously described (Orsini et al., 2012). Briefly, the score is composed of the assessment of several subtests of both global and focal deficits. Assessment of global deficits included grooming, status of ears and eyes, posture, spontaneous activity, and epileptic behavior. Focal deficits were evaluated by gait, grip, forelimb asymmetry during tail suspension, circling behavior of the entire body or only a forelimb, body symmetry, and whisker response. Total score ranges from 0 to 54 points (26 points for general and 28 for focal deficits), with a higher score indicating worse deficits. Data were acquired once before stroke and on days 3, 7, 14, 21, 28, 42, 56, 70, and 84 after stroke.

Cylinder test

The cylinder test was assessed as previously described (Llovera et al., 2014). Briefly, the animals were placed in a transparent acrylic glass cylinder (diameter, 8 cm; height, 25 cm) in front of two mirrors, and video was recorded for 10 min. The frequency of forelimb use during a full rear and landing with only one forelimb was counted. At least 20 contacts for one forelimb were counted using slow-motion or frame-by-frame function. The ratio was calculated as the total number of left forelimb contacts divided by the total number of right forelimb contacts with the cylinder wall.

Flow cytometry

Mice were deeply anesthetized and perfused with 20 ml saline. Both brain and spleen were dissected, and blood was collected in EDTA tubes after cardiac puncture. For brain, both hemispheres were carefully removed, and cells were isolated by mechanical dissociation. Cell preparation and staining were performed as previously described (Llovera et al., 2017). Mononuclear cells were enriched using discontinuous Percoll gradients. Cell stainings were performed using the following antibodies: CD45-eF450 (1:250, 48–0451-82, clone: 30-F11; Invitrogen), CD3-FITC (1:250, 11–0032-82, clone: 17A2; Invitrogen), CD8-PE (1:250, 12–0081-82, clone: 53–6.7; Invitrogen), CD4-PerCP-Cy5 (1:250, 45–0042-82, clone: RM4-5; Invitrogen), TCRyd-APC (1:250, 118116, clone: GL3; BioLegend), NK1.1-PE-Cy7 (1:250, 25–5941-82, clone: PK136; Invitrogen), CD19-APC-Cy7 (1:250, 47–0193-82, clone: eBio1D3; Invitrogen), CD11b-PerCP-Cy5 (1:250, 45–0112-82, clone: M1/70; Invitrogen), MHCII-PE (1:250, 12–5322-81, clone: NIMR-4; eBioscience), Ly6C-APC (1:500, 17–5932-82, clone: HK1.4; eBioscience), Ly6G-PE-Cy7 (1:333, 25–5931-82, clone: RB6-8C5; eBioscience), and CD11c-APC-Cy7 (1:250, 117324, clone: N418; BioLegend). Stained cells were analyzed on a BD FACSVerse flow cytometer (BD Biosciences), and analysis was performed using FlowJo software (version 10.0).

For high-dimensional flow cytometry (Fig. 2, B and C), mice were injected i.v. with 3 µg CD45-APC-Cy7 (103116, clone: 30-F11; BioLegend), 3 min before transcardiac perfusion, to exclude blood contamination. Mononuclear cells were then isolated as described above. The samples were stained first with Zombie NIR Fixable Viability Kit (1:200; BioLegend) and surface markers, diluted in Brilliant Stain Buffer (BD Biosciences). The following antibodies were used: CXCR3-BV421 (1:100, 126522, clone: CXCR3-127; BioLegend), CD27-SB436 (1:100, 62–0271-82, clone: LG.7F9; eBioscience), CD69-BV480 (1:50, 746813, clone: H1.2F3; BD Biosciences), CD19-BV570 (1:200, 115535, clone: 6D5; BioLegend), CD11b-BV570 (1:200, 101233, clone: M1/70; BioLegend), PD-1-BV605 (1:100, 563059, clone: J43; BD Biosciences), CD62L-BV650 (1:100, 564108, clone MEL-14; BD Biosciences), TCR-γδ-BV750 (1:100, 746962, clone: GL3; BD Biosciences), CCR7-BV785 (1:100, 120127, clone: 4B12; BioLegend), CD44-AF532 (1:200, 58–0441-82, clone: IM7; eBioscience), CD127-PE-CF594 (1:100, 562419, clone: SB/199; BD Biosciences), NK1.1-AF700 (1:100, 56–5941-82, clone: PK136; eBioscience), CD8a-BV510 (1:200, 563068, clone: 53-6.7; BD Biosciences), CD3-FITC (1:200, 11–0032-82, clone: 17A2; eBioscience), KLRG1-PE (1:200, 138408, clone: 2F1/KLRG1; BioLegend), CD103-PE-Cy7 (1:200, 121426, clone: 2E7; BioLegend), CD4-PerCP-Cy5.5 (1:200, 45–0042-82, clone: RM4-5; eBioscience). For intracellular staining, Foxp3 / Transcription Factor Staining Buffer Set was used following the provider guidelines. The following antibodies

for intracellular staining were used: FoxP3-AF647 (1:100, 126408, clone: MF-14; BioLegend), T-bet-BV711 (1:100, 644820, clone: 4B10; BioLegend), ROR-γt-APC (1:100, 17–6981-82, clone B2D; eBioscience). Stained cells were analyzed on a Norther Light spectral flow cytometer (Cytek) and analysis performed by FlowJo software (version 10.0).

In vivo proliferation analysis

For analysis of in vivo cell proliferation, mice were treated with EdU (0.5 mg/ml; Invitrogen) in sucrose-enriched drinking water (5 g sucrose in 100 ml) for 7 d before saline perfusion. EdU was detected using a Click-iT EdU Alexa Fluor 647 Flow Cytometry Assay Kit (C10419; Invitrogen) following the manufacturer's instructions. Subsequently, FACS antibody staining was performed as described above using the following cell surface antibodies: CD11b-PE-Cy7 (1:250, 25–0112-82, clone: M1/70; Invitrogen), CD45-BV510 (1:250, 563891, clone: 30-F11; BD Biosciences), CD3-FITC (1:250, 11–0032-82, clone: 17A2; Invitrogen), CD19-eF450 (1:250, 48–0193-82, clone: eBio1D3; eBioscience), CD4-PerCP-Cy5.5 (1:250, 45–0042-82, clone: RM4-5; Invitrogen), and CD8-PE (1:250, Invitrogen, 12–0081-82, clone: 53–6.7). Stained cells were then analyzed on a BD FACSVerse flow cytometer (BD Biosciences), and analysis was performed using FlowJo software (version 10.0).

Pharmacokinetic analysis

To determine cellular anti-CD49d saturation levels, venous blood was collected in EDTA tubes after cardiac puncture, and mononuclear cells were enriched using a Histopaque-1077 gradient (Sigma-Aldrich). Cells were diluted to a concentration of 10^6 cells/ml and stained with a mouse anti-Rat IgG2b PE-conjugated secondary antibody (1:20, clone R2B-7C3; eBioscience) to detect cell-bound anti-CD49d for 30 min at 4°C. For determination of anti-CD49d saturation, cells were incubated with a saturating amount of anti-CD49d (10 µg/ml) for 30 min at room temperature and subsequently stained with the antibody as described above. Stained cells were then analyzed on a BD FACSVerse flow cytometer (BD Biosciences), and analysis was performed using FlowJo software (version 10.0). The anti-CD49d saturation level was then calculated as percentage of the mean fluorescence intensity (MFI) from in vivo bound anti-CD49d from the MFI of in vitro saturated cells by the following equation:

$$\text{anti} - \text{CD49d saturation} = \frac{\text{MFI in vivo } \textit{bound anti} - \textit{CD49d}}{\text{MFI in vitro saturated anti} - \text{CD49d}} \times 100.$$

The number of anti-CD49d molecules per cell was determined using a PE fluorescence quantitation kit (BD Quantibrite PE, #340495; BD Biosciences) following the manufacturer's instructions.

Mouse anti-rat IgG ELISA

To analyze neutralizing mouse anti-rat IgG antibodies in mice, we used a customized modification of a commercial ELISA (#88-50400; Thermo Fisher Scientific). Flat-bottom 96-well ELISA plates were coated overnight with the same rat anti-CD49d antibody (100 ng/ml) at 4°C as used for the in vivo treatment (clone PS/2, Cat. BE0071; Bio X Cell). After washing, the antibody-coated plates were incubated for 1 h at room temperature with mouse plasma obtained 28 d after stroke (i.e., two doses of anti-CD49d at 2 h and 14 d) or control plasma from a naive mouse that had been spiked at ∼10 ng/ml with the capture antibody of the ELISA kit. Subsequent detection and biochemiluminescent analysis using a microplate reader (Bio-Rad) was performed following the manufacturer's instructions.

Dendritic spine analysis

Following saline perfusion, mice were perfused 84 d after PT with aldehyde fixative solution (003780; Bioenno). Brains were then carefully removed and placed in fixative solution at 4°C overnight. Brains were then sliced at 100 µm using a vibratome and collected in 0.1 M PBS. Slices were placed in impregnation slice Golgi Kit (003760; Bioenno) solution for 5 d in the dark. Staining and post-staining was performed as described by the manufacturer (Bioenno). Images of dendrites were obtained within 500 µm around the lesion area in cortical layer 2/3. In total, 25 dendrites per animal (5 dendrites from 5 neurons) in both hemispheres were recorded using an Axio Imager.M2 and a 100× objective (EC Plan-Neofluar, numerical aperture [NA] = 1.3, oil immersion, acquisition at 18–20°C) using the AxioCam MRc and AxioVision 4.8.2 software. Dendrites from the images were then 3D reconstructed and the spine density evaluated on the reconstructed 3D surface using Imaris x64 (8.4.0; Bitplane).

In vivo widefield neuronal calcium imaging

In vivo widefield calcium imaging was performed as previously published (Cramer et al., 2019b). Briefly, Thy1-GCaMP6s heterozygous mice were scalped and transparent dental cement was placed upon the intact skull at least 3 d before start of the experiment. Resting-state in vivo imaging was performed in mild anesthesia (0.5 mg/kg body weight of medetomidine with 0.75% isoflurane inhalation). Mice were placed in a stereotactic frame below a customized macroscopic imaging setup, and mouse cortex was illuminated with 450-nm blue LED light. Resting-state calcium activity was recorded for 4 min (6 × 1,000 frames) with a high-precision 2/3" Interline charge-coupled device camera (Adimec-1000m/D, pixel size 7.4 × 7.4 µm, acquisition at 20–22°C; Adimec) at a 25-Hz frame rate using longDaq software (Optical Imaging).

In vivo calcium imaging analysis

Functional imaging data were preprocessed as previously described (Cramer et al., 2019b). In particular, the seed-to-seed FCs between eight previously defined seeds were calculated as Pearson's correlation between the time course of each of these seeds and Fisher's z transformation. For left intrahemispheric connectivity, the mean of the Fisher's z-transformed Pearson's correlation coefficient of each connection between the seeds located in the left hemisphere was calculated. The overall homotopic connectivity was calculated as the mean of all Fisher's z-transformed Pearson's correlation coefficients of each homotopic connection between the seeds in both hemispheres. The time course of left intrahemispheric and overall homotopic

connectivity was displayed from baseline and days 42 to 84 after stroke, ensuring the visibility of all seeds after disappearance of the autofluorescent lesion. Fisher's z-transformed Pearson's correlation was calculated using MATLAB (MathWorks R2016b with Optimization Toolbox, Statistics and Machine Learning Toolbox, Signal Processing Toolbox and Image Processing Toolbox; MathWorks).

Lesion involution quantification

The lesion size was determined by autofluorescence of the ischemic tissue in Thy1-GCaMP6s animals used for in vivo widefield calcium imaging for every time point of imaging acquisition. The area of autofluorescent pixels was previously defined by thresholding and converted into a mask to exclude autofluorescent tissue from the connectivity analysis. The lesion was determined as the size of the exclusion mask by quantification of all pixels within the mask.

Lesion volumetry

Mice were transcardially perfused 28 d after PT or dMCAo stroke induction with saline and 4% paraformaldehyde solution. To protect the cortical lesion from damage, the whole skull was isolated and stored in 4% paraformaldehyde overnight at 4°C and then placed in 0.3 M EDTA for 7 d for decalcification. Subsequently, the brains were dehydrated for 2 d in 30% sucrose in 0.01 M PBS and then snap-frozen in isopentane. Cresyl Violet staining for infarct volumetry was performed as previously described (Llovera et al., 2014), and the lesion size was quantified using FIJI ImageJ.

Immunohistochemical staining of mouse coronal brain sections

Fluorescent immunohistochemical staining for $CD3^+$ and $Ki67^+$ to determine the number of proliferating T cells in control versus anti-CD49d treated animals was performed on 20-µm-thick paraformaldehyde-fixed coronal sections from mice at 7 and/or 28 d after PT or dMCAo. Sections were fixed with cold acetone for 10 min at room temperature and washed with 0.01 M PBS before blocking with goat serum blocking buffer for 1 h at room temperature. Subsequently, sections were stained overnight at 4°C with primary antibody (1:200, CD3e, hamster anti-mouse, clone 500A2; BD PharMingen; and 1:200, Ki-67, rabbit mAb, clone D3B5; Cell Signaling Technology). After washing with 0.1% Triton X-100 in 0.01 M PBS, secondary antibody staining was applied for 2 h at room temperature (1:200, goat anti-hamster, Alexa Fluor 594; Thermo Fisher Scientific; and 1:200, goat anti-rabbit, Alexa Fluor 647; Life Technologies). Nuclei were stained with DAPI (1:5,000; Invitrogen) for 5 min at room temperature.

Per animal, three images for cell quantification were recorded as 6-µm-high tile-scan Z-stacks (slice thickness, 0.4 µm) on a Zeiss confocal microscope (LSM880) with 25× objective (LCI Plan-Neofluar 25×, NA = 0.8, ImmKorr differential interference contrast, water immersion, acquisition at 18°C). The lesion was marked and measured in the tile-scan image and cells were quantified using the Cell Counter Plugin in FIJI. Cell density was calculated as number of cells per square millimeter. The R index for quantification of clustering of cells per area was calculated using the clarkevans.test R function (R package spatstat; Baddeley et al., 2005). For evaluation of clustering, the ratio of the observed average nearest-neighbor distance r (rA) to the expected pattern for a Poisson point process of the same intensity (rE): $R=\frac{rA}{rE}$. An R index of >1.0 indicates ordered spatial distribution, R = 0 indicates even distribution, and R < 1.0 indicates aggregation. Hypothesis testing was performed against the null hypothesis, which is complete spatial randomness/a uniform Poisson process. For every animal, the cell density and R index were calculated and averaged among the three acquired images. Whole-slice images were acquired using a 10× objective (EC Plan-Neofluar 10×, NA = 0.3, air immersion, acquisition at 18°C) and high-resolution images were acquired using a 40× objective (EC Plan-Neofluar 40×, NA = 1.3 oil differential interference contrast, oil immersion, acquisition at 18–20°C).

Patient characteristics for postmortem histological analyses

Ethical approval for the use of human postmortem material was granted according to institutional ethics board protocol and national regulations by the Hungarian Medical Research Council Scientific and Research Ethics Board (19312/2016/EKU) and the University of Kentucky Medical Institutional Review Board (UK IRB #44009), respectively. Clinical information was provided by the respective brain bank (Table S1).

Histological and immunohistochemical staining of human brain tissue samples

Histochemical and immunohistochemical staining was performed on sections cut to 6 µm from paraffin-embedded tissue blocks. Randomly chosen sections of every patient were deparaffinated and rehydrated and subsequently stained with H&E. Immunohistochemistry for CD3 (polyclonal rabbit anti-human CD3, diluted 1:50, A0452; Dako) was performed on sections adjacent to H&E-stained sections with the Ventana Benchmark GX automated staining system using a CC1 (Roche) pretreatment and the iView DAB Detection Kit (Roche). Sections were counterstained with hematoxylin and coverslipped with Entellan (Merck) as mounting medium. Age of infarcts was estimated by two experienced and independent neuropathologists (T. Arzberger and P.T. Nelson) on H&E sections according to published criteria (Mena et al., 2004). CD3 stains were scanned with Zeiss Axio Scan Z1 using a 20× objective. The infarct area was demarcated, and the absolute numbers and coordinates of intra- and extralesional $CD3^+$ T cells were assessed manually using Qupath (version 0.2.2). Cell density was calculated as number of cells per cm^2 of defined lesion area. The R index for quantification of cell clustering per area was calculated as described above in R (version 3.6.0). Intralesional cell density was correlated with time after stroke onset for each sample.

Immunofluorescence staining of human brain tissue samples

Immunofluorescence staining was performed on sections cut to 6 µm from paraffin-embedded tissue blocks. Randomly selected sections were deparaffinated and blocked in 3% H_2O_2. After heat-induced antigen retrieval in Tris-buffered EDTA (pH 9.0) for 30 min at 95°C, sections were blocked with 5% donkey serum for 4 h at room temperature. Then, sections were incubated in

antibody staining solution (0.3% Triton X-100 and 20 mM sodium azide containing 0.05 M Tris-buffered saline [TBS], pH 7.4) overnight at 4°C (1:50, CD3, polyclonal rabbit anti-human, reference A0452; and 1:100, Ki67, monoclonal mouse anti-human, clone MIB-1, reference M7240; Dako). After washing with 0.05 M TBS, secondary antibody staining was performed with antibody staining solution (0.3% Triton X-100 and 20 mM sodium azide containing 0.05 M TBS, pH 7.4) for 2.5 h at room temperature in the dark (1:500, donkey anti-rabbit, Alexa Fluor 594, reference 711–586-152; and 1:500, donkey anti-mouse, Alexa Fluor 488, reference 715–546-151; Jackson ImmunoResearch). For nuclear staining, Hoechst 33334 (0.02 mg/ml diluted in 0.05 M TBS, pH 7.4, reference 62249; Thermo Fisher Scientific) was applied for 30 min at room temperature. After staining, an autofluorescence eliminator reagent (reference 2160; EMD Millipore) was applied for 5 min before mounting the slides with Fluoromount-G (reference 0100–01; Southern Biotech). The images were acquired at 20× magnification (objective: Plan Apo VC 20×, NA = 0.75, working distance = 1 mm, field of view = 645.12 µm, calibration: 0.62 µm/pixel or with 5× optical zoom, calibration: 0.12 µm/pixel, acquisition at 21°C) using a Nikon Ni C2 confocal microscope.

Statistics

To assess whether the lesion involution (number of autofluorescent pixels), behavioral recovery (neuroscore and cylinder test) or FC (left intra-FC and overall homotopic FC) between anti-CD49d–treated and control-treated animals were significantly different, we performed linear-mixed models for calculating group-by-time interaction in R (version 3.6.0). To test for statistical difference in infarct volume between treatment groups, we used one-way ANOVA and Tukey's post-hoc test. Next, we assessed the difference in dendritic spine numbers between anti-CD49d–treated and control-treated animals using the Wilcoxon rank-sum test with continuity correction and Bonferroni post-hoc correction for multiple testing in R (Version 3.6.0). To test for significantly different numbers of infiltrating T cells between anti-CD49d– and control-treated animals, we used unpaired *t* tests and Holm–Sidak's correction for multiple testing. For determining significant differences in histologically quantified T cells, we used an unpaired *t* test. To assess significant differences in the R index between treatment groups at different time points, we used one-way ANOVA and Tukey's test for correction of multiple comparisons. We next quantified significant differences between the number of EdU^+ T cells in different organs using one-way ANOVA and Tukey's test for correction of multiple comparisons. To test for significant differences in the percentage of $Ki67^+$ T cells between treatment groups, we used an unpaired *t* test. We used linear regression analysis to test for a correlation between the intralesional T cell density in stroke patients and time after stroke onset. Unless otherwise mentioned all analyses were performed in GraphPad Prism (version 7.0a). For all analyses, an α level of adjusted $P < 0.05$ was considered statistically significant.

Online supplemental material

Fig. S1 provides pharmacokinetic analysis data for the rationale of the treatment regimen with anti-CD49d and additional results on infarct volumetry supporting the findings in the Fig. 1 in the PT and dMCAo stroke model. Fig. S2 provides information on the temporal dynamics of cerebral invasion on innate and adaptive immune subpopulations over 1 mo after experimental stroke. Fig. S3 shows comparable findings for chronic T cell accumulation in female mice as shown in the main figures for male mice. Additionally, this figure confirms chronic T cell accumulation and proliferation in the dMCAo stroke model. Table S1 lists patient data.

Acknowledgments

We would like to thank Kerstin Thuβ-Silczak and Christina Fürle for technical support as well as Juliet Stowe for the selection and preparation of human tissue samples from the Sanders Brown Center on Aging (supported by National Institutes of Health grant P30 AG028383).

This work was funded by the European Research Council (grant ERC-StGs 802305 to A. Liesz and grant ERC-PoC 875677 to D. Edbauer), the American Heart Association (grant 19EIA34760279 to A.M. Stowe), the Hungarian Brain Research Program (grant 2017-1.2.1-NKP-2017-00002), and the German Research Foundation under Germany's Excellence Strategy (EXC 2145 SyNergy, ID 390857198) through the collaborative research center TRR274 (project ID 408885537) and under grants LI-2534/6-1 and LI-2534/7-1. D. Edbauer received funding from the NOMIS Foundation.

Author contributions: S. Heindl conceptualized experiments, performed most of the experiments, analyzed the data, and wrote the manuscript. A. Ricci performed and analyzed experiments. O. Carofiglio, Q. Zhou, T. Arzberger, and N. Lenart performed experiments. N. Franzmeier analyzed FC data. T. Hortobagyi, P.T. Nelson, A.M. Stowe, and A. Denes selected and provided the human tissue samples. D. Edbauer provided experimental resources. A. Liesz initiated the study, conceptualized and supervised the research, and wrote the manuscript. All authors reviewed the manuscript.

Disclosures: The authors declare no competing interests exist.

Submitted: 11 November 2020
Revised: 31 March 2021
Accepted: 28 April 2021

References

Baddeley, A., E. Rubak, and R. Turner. 2005. Spatial Point Patterns: Methodology and Applications with R. Chapman and Hall/CRC Press, London.

Becker, K., D. Kindrick, J. Relton, J. Harlan, and R. Winn. 2001. Antibody to the alpha4 integrin decreases infarct size in transient focal cerebral ischemia in rats. *Stroke.* 32:206–211. https://doi.org/10.1161/01.STR.32.1.206

Chamorro, Á., A. Meisel, A.M. Planas, X. Urra, D. van de Beek, and R. Veltkamp. 2012. The immunology of acute stroke. *Nat. Rev. Neurol.* 8:401–410. https://doi.org/10.1038/nrneurol.2012.98

Cotrina, M.L., N. Lou, J. Tome-Garcia, J. Goldman, and M. Nedergaard. 2017. Direct comparison of microglial dynamics and inflammatory profile in photothrombotic and arterial occlusion evoked stroke. *Neuroscience.* 343:483–494. https://doi.org/10.1016/j.neuroscience.2016.12.012

Cramer, J.V., C. Benakis, and A. Liesz. 2019a. T cells in the post-ischemic brain: Troopers or paramedics? *J. Neuroimmunol.* 326:33–37. https://doi.org/10.1016/j.jneuroim.2018.11.006

Cramer, J.V., B. Gesierich, S. Roth, M. Dichgans, M. Düring, and A. Liesz. 2019b. In vivo widefield calcium imaging of the mouse cortex for analysis of network connectivity in health and brain disease. *Neuroimage.* 199:570–584. https://doi.org/10.1016/j.neuroimage.2019.06.014

Cserép, C., B. Pósfai, N. Lénárt, R. Fekete, Z.I. László, Z. Lele, B. Orsolits, G. Molnár, S. Heindl, A.D. Schwarcz, et al. 2020. Microglia monitor and protect neuronal function through specialized somatic purinergic junctions. *Science.* 367:528–537. https://doi.org/10.1126/science.aax6752

Dana, H., T.W. Chen, A. Hu, B.C. Shields, C. Guo, L.L. Looger, D.S. Kim, and K. Svoboda. 2014. Thy1-GCaMP6 transgenic mice for neuronal population imaging in vivo. *PLoS One.* 9:e108697. https://doi.org/10.1371/journal.pone.0108697

Doyle, K.P., L.N. Quach, M. Solé, R.C. Axtell, T.-V.V. Nguyen, G.J. Soler-Llavina, S. Jurado, J. Han, L. Steinman, F.M. Longo, et al. 2015. B-lymphocyte-mediated delayed cognitive impairment following stroke. *J. Neurosci.* 35:2133–2145. https://doi.org/10.1523/JNEUROSCI.4098-14.2015

Elkind, M.S.V., R. Veltkamp, J. Montaner, S.C. Johnston, A.B. Singhal, K. Becker, M.G. Lansberg, W. Tang, R. Kasliwal, and J. Elkins. 2020. Natalizumab in acute ischemic stroke (ACTION II): A randomized, placebo-controlled trial. *Neurology.* 95:e1091–e1104. https://doi.org/10.1212/WNL.0000000000010038

Elkins, J., R. Veltkamp, J. Montaner, S.C. Johnston, A.B. Singhal, K. Becker, M.G. Lansberg, W. Tang, I. Chang, K. Muralidharan, et al. 2017. Safety and efficacy of natalizumab in patients with acute ischaemic stroke (ACTION): a randomised, placebo-controlled, double-blind phase 2 trial. *Lancet Neurol.* 16:217–226. https://doi.org/10.1016/S1474-4422(16)30357-X

Emberson, J., K.R. Lees, P. Lyden, L. Blackwell, G. Albers, E. Bluhmki, T. Brott, G. Cohen, S. Davis, G. Donnan, et al. Stroke Thrombolysis Trialists' Collaborative Group. 2014. Effect of treatment delay, age, and stroke severity on the effects of intravenous thrombolysis with alteplase for acute ischaemic stroke: a meta-analysis of individual patient data from randomised trials. *Lancet.* 384:1929–1935. https://doi.org/10.1016/S0140-6736(14)60584-5

Endres, M., B. Engelhardt, J. Koistinaho, O. Lindvall, S. Meairs, J.P. Mohr, A. Planas, N. Rothwell, M. Schwaninger, M.E. Schwab, et al. 2008. Improving outcome after stroke: overcoming the translational roadblock. *Cerebrovasc. Dis.* 25:268–278. https://doi.org/10.1159/000118039

Fiehler, J., and C. Gerloff. 2015. Mechanical Thrombectomy in Stroke. *Dtsch. Arztebl. Int.* 112:830–836.

Hacke, W., M. Kaste, E. Bluhmki, M. Brozman, A. Dávalos, D. Guidetti, V. Larrue, K.R. Lees, Z. Medeghri, T. Machnig, et al. ECASS Investigators. 2008. Thrombolysis with alteplase 3 to 4.5 hours after acute ischemic stroke. *N. Engl. J. Med.* 359:1317–1329. https://doi.org/10.1056/NEJMoa0804656

Howells, D.W., E.S. Sena, and M.R. Macleod. 2014. Bringing rigour to translational medicine. *Nat. Rev. Neurol.* 10:37–43. https://doi.org/10.1038/nrneurol.2013.232

Iadecola, C., and J. Anrather. 2011. The immunology of stroke: from mechanisms to translation. *Nat. Med.* 17:796–808. https://doi.org/10.1038/nm.2399

Kilkenny, C., W.J. Browne, I.C. Cuthill, M. Emerson, and D.G. Altman. 2010. Improving bioscience research reporting: the ARRIVE guidelines for reporting animal research. *PLoS Biol.* 8:e1000412. https://doi.org/10.1371/journal.pbio.1000412

Langhauser, F., P. Kraft, E. Göb, J. Leinweber, M.K. Schuhmann, K. Lorenz, M. Gelderblom, S. Bittner, S.G. Meuth, H. Wiendl, et al. 2014. Blocking of α4 integrin does not protect from acute ischemic stroke in mice. *Stroke.* 45:1799–1806. https://doi.org/10.1161/STROKEAHA.114.005000

Liesz, A., E. Suri-Payer, C. Veltkamp, H. Doerr, C. Sommer, S. Rivest, T. Giese, and R. Veltkamp. 2009. Regulatory T cells are key cerebroprotective immunomodulators in acute experimental stroke. *Nat. Med.* 15:192–199. https://doi.org/10.1038/nm.1927

Liesz, A., W. Zhou, É. Mracskó, S. Karcher, H. Bauer, S. Schwarting, L. Sun, D. Bruder, S. Stegemann, A. Cerwenka, et al. 2011. Inhibition of lymphocyte trafficking shields the brain against deleterious neuroinflammation after stroke. *Brain.* 134:704–720. https://doi.org/10.1093/brain/awr008

Llovera, G., S. Roth, N. Plesnila, R. Veltkamp, and A. Liesz. 2014. Modeling stroke in mice: permanent coagulation of the distal middle cerebral artery. *J. Vis. Exp.* (89):e51729. https://doi.org/10.3791/51729

Llovera, G., K. Hofmann, S. Roth, A. Salas-Pérdomo, M. Ferrer-Ferrer, C. Perego, E.R. Zanier, U. Mamrak, A. Rex, H. Party, et al. 2015. Results of a preclinical randomized controlled multicenter trial (pRCT): Anti-CD49d treatment for acute brain ischemia. *Sci. Transl. Med.* 7:299ra121. https://doi.org/10.1126/scitranslmed.aaa9853

Llovera, G., C. Benakis, G. Enzmann, R. Cai, T. Arzberger, A. Ghasemigharagoz, X. Mao, R. Malik, I. Lazarevic, S. Liebscher, et al. 2017. The choroid plexus is a key cerebral invasion route for T cells after stroke. *Acta Neuropathol.* 134:851–868. https://doi.org/10.1007/s00401-017-1758-y

Macleod, M.R., S. Michie, I. Roberts, U. Dirnagl, I. Chalmers, J.P. Ioannidis, R. Al-Shahi Salman, A.W. Chan, and P. Glasziou. 2014. Biomedical research: increasing value, reducing waste. *Lancet.* 383:101–104. https://doi.org/10.1016/S0140-6736(13)62329-6

Macrez, R., C. Ali, O. Toutirais, B. Le Mauff, G. Defer, U. Dirnagl, and D. Vivien. 2011. Stroke and the immune system: from pathophysiology to new therapeutic strategies. *Lancet Neurol.* 10:471–480. https://doi.org/10.1016/S1474-4422(11)70066-7

Mena, H., D. Cadavid, and E.J. Rushing. 2004. Human cerebral infarct: a proposed histopathologic classification based on 137 cases. *Acta Neuropathol.* 108:524–530. https://doi.org/10.1007/s00401-004-0918-z

Moskowitz, M.A., E.H. Lo, and C. Iadecola. 2010. The science of stroke: mechanisms in search of treatments. *Neuron.* 67:181–198. https://doi.org/10.1016/j.neuron.2010.07.002

Neumann, J., M. Riek-Burchardt, J. Herz, T.R. Doeppner, R. König, H. Hütten, E. Etemire, L. Männ, A. Klingberg, T. Fischer, et al. 2015. Very-late-antigen-4 (VLA-4)-mediated brain invasion by neutrophils leads to interactions with microglia, increased ischemic injury and impaired behavior in experimental stroke. *Acta Neuropathol.* 129:259–277. https://doi.org/10.1007/s00401-014-1355-2

Orsini, F., P. Villa, S. Parrella, R. Zangari, E.R. Zanier, R. Gesuete, M. Stravalaci, S. Fumagalli, R. Ottria, J.J. Reina, et al. 2012. Targeting mannose-binding lectin confers long-lasting protection with a surprisingly wide therapeutic window in cerebral ischemia. *Circulation.* 126:1484–1494. https://doi.org/10.1161/CIRCULATIONAHA.112.103051

Relton, J.K., K.E. Sloan, E.M. Frew, E.T. Whalley, S.P. Adams, and R.R. Lobb. 2001. Inhibition of alpha4 integrin protects against transient focal cerebral ischemia in normotensive and hypertensive rats. *Stroke.* 32:199–205. https://doi.org/10.1161/01.STR.32.1.199

Sadler, R., J.V. Cramer, S. Heindl, S. Kostidis, D. Betz, K.R. Zuurbier, B.H. Northoff, M. Heijink, M.P. Goldberg, E.J. Plautz, et al. 2020. Short-Chain Fatty Acids Improve Poststroke Recovery via Immunological Mechanisms. *J. Neurosci.* 40:1162–1173. https://doi.org/10.1523/JNEUROSCI.1359-19.2019

World Health Organization. 2017. Top 10 Causes of Death. In World Health Organization. World Health Organization, Geneva.

Zhou, W., A. Liesz, H. Bauer, C. Sommer, B. Lahrmann, N. Valous, N. Grabe, and R. Veltkamp. 2013. Postischemic brain infiltration of leukocyte subpopulations differs among murine permanent and transient focal cerebral ischemia models. *Brain Pathol.* 23:34–44. https://doi.org/10.1111/j.1750-3639.2012.00614.x

Supplemental material

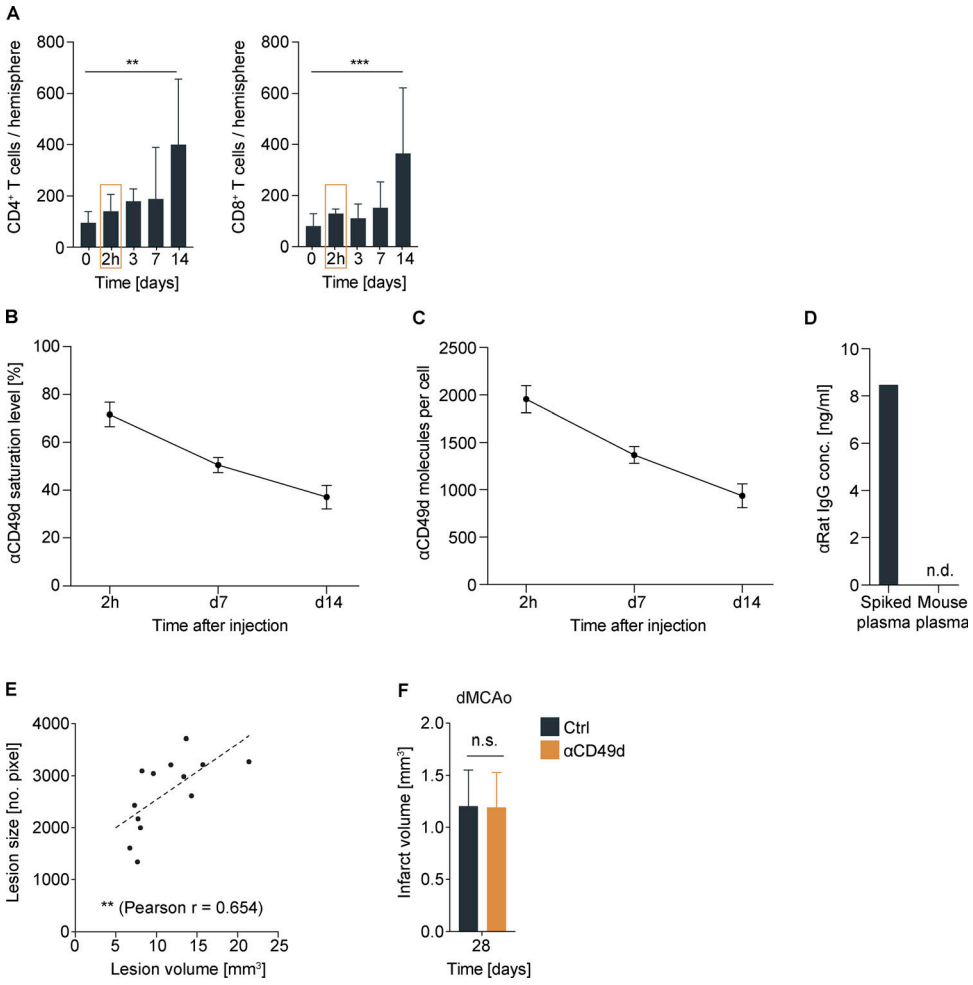

Figure S1. **Rationale for anti-CD49d treatment regimen and infarct volumetric assessment. (A)** Flow cytometric analysis of acute CD4⁺ and CD8⁺ T cell infiltration into the ipsilateral hemisphere after photothrombosis; *n* (0 = sham) = 10, *n* (2 h) = 3, *n* (3 d) = 6, *n* (7 d) = 6, *n* (14 d) = 5. Data are shown as mean + SD; ordinary one-way ANOVA + Dunnett's post-hoc test. At least two independent experiments were performed per time point in WT animals. **(B)** Saturation levels of anti-CD49d measured at 2 h and 7 and 14 d after i.p. injection of 300 µg anti-CD49d per animal; *n* = 3–4 per time point. Data are shown as mean + SD. Data were acquired in at least two independent experiments in WT animals. **(C)** Quantification of anti-CD49d molecules bound per cell at 2 h and 7 and 14 d after anti-CD49d treatment; *n* = 3–4 per time point. Data were acquired in at least two independent experiments in WT animals. **(D)** Mouse plasma concentration of anti-rat IgG is shown at day 28 from mice receiving two injections of 300 µg anti-CD49d at 2 h and 14 d after stroke. Naive mouse plasma was spiked with monoclonal anti-rat IgG as a positive control (spiked plasma); *n* = 3. **(E)** Correlation of lesion volume (histological analysis) and lesion size (autofluorescent pixels). Pearson correlation *n* = 13. Data were acquired in two independent experiments in Thy1GCaMP6s animals. **(F)** Infarct volume 28 d after distal middle cerebral occlusion; *n* (control) = 6, *n* (αCD49d) = 5. Data are shown as mean + SD. Unpaired *t* test. Data were acquired in three independent experiments in WT animals. **, P < 0.01; ***, P < 0.001.

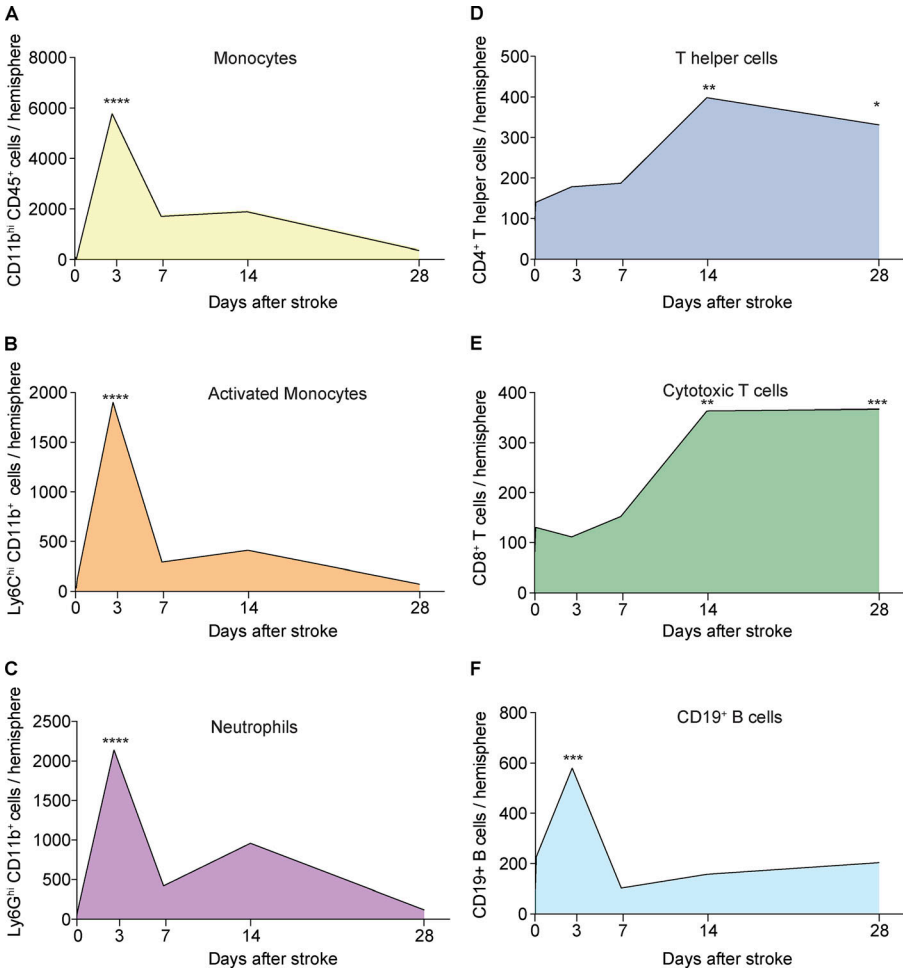

Figure S2. **Temporal dynamics of myeloid and lymphoid immune cell infiltration after stroke. (A–F)** Absolute counts of monocytes (A), activated monocytes (B), neutrophils (C), CD4$^+$ T helper cells (D), CD8$^+$ cytotoxic T cells (E), and CD19$^+$ B cells (F) were assessed using flow cytometry at 2 h and 3–28 d after stroke, as well as after sham surgery (day 0) in the ipsilateral hemisphere; *n* (sham) = 10, *n* (2 h) = 3, *n* (3 d) = 5–6, *n* (7 d) = 5–6, *n* (14 d) = 5, *n* (28 d) = 5. Mean values are shown per time point. Ordinary one-way ANOVA + Dunnett's post-hoc test. At least two independent experiments were performed per time point in WT animals. *, P < 0.05; **, P < 0.01; ***, P < 0.001; ****, P < 0.0001.

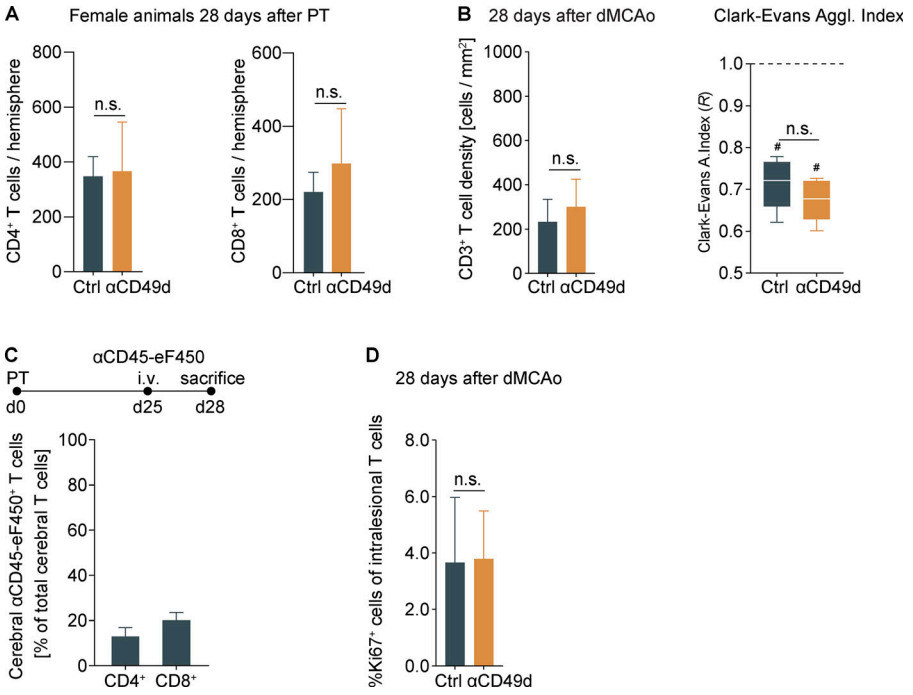

Figure S3. **Chronic T cell accumulation in female mice and after dMCAo. (A)** Flow cytometric analysis of CD4⁺ and CD8⁺ T cells 28 d after stroke in female mice; *n* = 7–8 per group, unpaired *t* test. Data are shown as mean + SD. **(B)** Evaluation of cell density and cell agglomeration of CD3⁺ intralesional T cells 28 d after dMCAo; *n* = 5 per group, unpaired *t* test. Data are shown as mean + SD/median and interquartile range. **(C)** i.v. labeling of circulating CD45⁺ leukocytes over 3 d before flow cytometric brain analysis 28 d after stroke reveals only a small fraction of brain-invading CD4⁺ and CD8⁺ T cells out of total cerebral T cells in the ischemic hemisphere; *n* = 4. Data are shown as mean + SD. **(D)** Percentage of Ki67⁺ T cells 28 d after dMCAo; *n* = 5 per group, unpaired *t* test. Data are shown as mean + SD. All data were generated in three independent experiments in WT animals. #, P < 0.05 for R < 1.0.

Table S1 is provided online as a Word document and lists patient data.